Single-Phase Microscale Jet Stagnation Point Heat Transfer

Gregory J. Michna[1]
e-mail: michng@rpi.edu

Eric A. Browne

Yoav Peles

Michael K. Jensen

Department of Mechanical, Aerospace, and Nuclear Engineering,
Rensselaer Polytechnic Institute,
Troy, NY 12180

An investigation of the pressure drop and impingement zone heat transfer coefficient trends of a single-phase microscale impinging jet was undertaken. Microelectromechanical system (MEMS) processes were used to fabricate a device with a 67-μm orifice. The water jet impinged on an 80-μm square heater on a normal surface 200 μm from the orifice. Because of the extremely small heater area, the conjugate convection-conduction heat transfer process provided an unexpected path for heat losses. A numerical simulation was used to estimate the heat losses, which were quite large. Pressure loss coefficients were much higher in the range $Re_{d,o}<500$ than those predicted by available models for short orifice tubes; this behavior was likely due to the presence of the wall onto which the jet impinged. At higher Reynolds numbers, much better agreement was observed. Area-averaged heat transfer coefficients up to 80,000 W/m^2 K were attained in the range $70<Re_d<1900$. This corresponds to a 400 W/cm^2 heat flux at a 50°C temperature difference. However, this impingement zone heat transfer coefficient is nearly an order-of-magnitude less than that predicted by correlations developed from macroscale jet data, and the dependence on the Reynolds number is much weaker than expected. Further investigation of microjet heat transfer is needed to explain the deviation from expected behavior. [DOI: 10.1115/1.3154750]

Keywords: electronics cooling, microscale jet heat transfer, microjet, orifice pressure loss coefficient

1 Introduction

Due to the increasing power consumption and decreasing size of electronic chips, cooling of these devices is becoming increasingly difficult. Heat fluxes seen in processors and power electronics are quickly approaching levels that cannot be easily accommodated by forced air convection over finned heat sinks. Therefore, more effective heat transfer cooling methods will be necessary to meet heat rejection needs within the next few years. One approach being investigated is liquid cooling, which takes advantage of a liquid's high (compared with air) conductivity, Prandtl number, density, and specific heat; because of these advantages, there have been many recent investigations of the use of liquid microchannel flows for electronics cooling.

Another possible liquid cooling method is microscale jet impingement cooling. Jet impingement cooling offers high heat transfer coefficients and has been used effectively in conventional-scale applications such as turbine blade cooling and the quenching of metals. Many studies investigating the performance of circular macroscale jets are available in the literature. Reviews of the single-phase heat and mass transfer performance of circular macroscale jets were given by Martin [1] and Jambunathan et al. [2].

Less information is available concerning the heat transfer performance of microscale jets. There have been several investigations of the performance of arrays of microscale jets [3–8] but very few published studies describing the heat transfer performance of a single circular microscale impinging jet.

Wu et al. [9] performed experiments investigating the heat transfer characteristics of a single confined submerged compressed-air jet with diameters between 500 μm and 1500 μm. They reported a heat transfer coefficient of 320 W/m^2 K for a 500-μm diameter jet with a standoff (the distance from orifice exit to heated surface) of 750 μm and a pressure drop of 5 psi. Reynolds numbers were not reported. The heat transfer coefficient was very small because the entire 2 cm $\times$ 2 cm chip was taken to be the heat transfer area, and the 500-μm diameter jet had little influence over most of this area.

Patil and Narayanan [10] performed an experimental study of a confined submerged 125-μm circular air jet. Spatially resolved heat transfer data were obtained using an infrared radiometer to measure the temperature of the heated thin foil onto which the jet impinged. Reynolds numbers in these experiments were in the range $700<Re_d<1800$. Standoff-to-diameter ratios of 2, 4, and 6 were tested, and the heat transfer coefficients were determined to be insensitive to this ratio in that range. The stagnation point Nusselt number varied from about $Nu_d=15$ at $Re_d=700$ to $Nu_d=55$ at $Re_d=1800$. The area-averaged Nusselt number results were compared with those predicted by the correlation given by Martin [1]. The observed area-averaged Nusselt numbers were approximately 40% lower than predicted at Reynolds numbers (based on orifice diameter) less than 1000, and approximately 25% higher than predicted at Reynolds numbers greater than 1700.

The pressure drop across the microjet orifice is also of interest to obtain a better understanding of the overall system and when considering pumping requirements. The microjet papers discussed above do not contain detailed information about the pressure drops across the orifices; however, there are several recent investigations of the pressure drop of flow through short microtubes or orifice tubes [11–13], the conclusions of which may be applicable to microjet orifice flows. Jankowski et al. [13] developed a model to predict the pressure drop for incompressible flows through orifices, including micro-orifices, with length-to-diameter ratios in the range $0<L/d<15$ and Reynolds numbers in the range $0<Re_{d,o}<3000$.

In this work, we examine the performance of a single-phase 67-μm diameter confined submerged impinging jet of water. The pressure drops and heat transfer coefficients are studied using a device fabricated using standard microelectromechanical system (MEMS) procedures. The pressure loss coefficients across the orifice are investigated. Using a heated section that measures only

[1]Corresponding author.

Contributed by the Heat Transfer Division of ASME for publication in the JOURNAL OF HEAT TRANSFER. Manuscript received January 16, 2009; final manuscript received May 4, 2009; published online August 26, 2009. Review conducted by Jayathi Murthy.

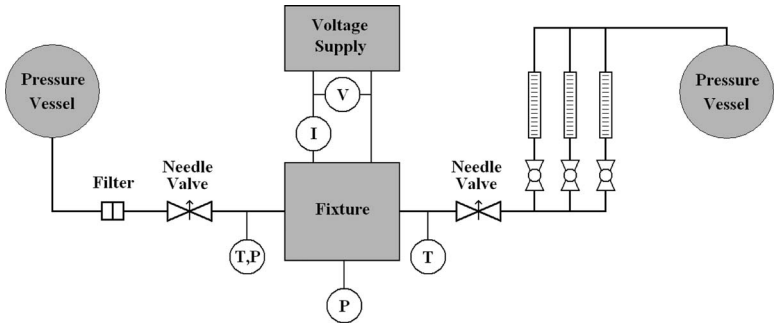

Fig. 1 Schematic of the flow loop used in the experiments

80 μm $\times$ 80 μm, area-averaged Nusselt numbers are determined. These area-averaged Nusselt numbers correspond to the so-called impingement zone, a region very close to the jet stagnation point.

2 Experimental Apparatus and Method

2.1 Apparatus. The experimental apparatus consisted of an open flow loop delivering water to and from a microdevice. A fixture was designed and built to incorporate the microdevice, fabricated using MEMS fabrication processes in a clean room environment, into the flow loop as well as to provide electrical contact. The working fluid was degassed de-ionized water.

The flow loop (Fig. 1) contains two tanks: one that supplies fluid to the device and one that collects fluid from the device exit. The flow traveled from the supply tank through a filter and needle valve before entering the fixture and microdevice. After exiting the microdevice, the flow traveled through another needle valve to one of three rotameters used to measure the flow rate before being discarded in the receiving tank. Three rotameters with different flow ranges were used to allow for a wide range of flow conditions; valves were used to direct all of the flow through each rotameter as needed. Type-T thermocouples were located before and after the fixture. Absolute pressure transducers were connected to the fluid entrance of the fixture and the chamber pressure port in the device.

A fixture (Fig. 2) was designed to integrate the device into the experimental apparatus. The fixture was fabricated with a computer numerical control (CNC) mill to ensure an accurate fit with the microdevice. A pocket was cut into the top surface of a Delrin block to hold the microdevice. Fluid channels were drilled into the Delrin fixture in the locations of the orifice, the pressure tap, and the device fluid exits. These locations were sealed with rubber o-rings seated in recesses in the fixture. Two spring-loaded pins were press fit into the fixture from below and were extended above the mating surface to the contact pads on the device. These pins were connected to an Instek PSP-405 power supply. Two HP 3457A multimeters were connected to measure the current and voltage supplied to the heater. A thin aluminum plate was bolted to the top of the fixture to hold the device in place and to ensure proper sealing of the fluid ports and good electrical contact between the pins and the contact pads.

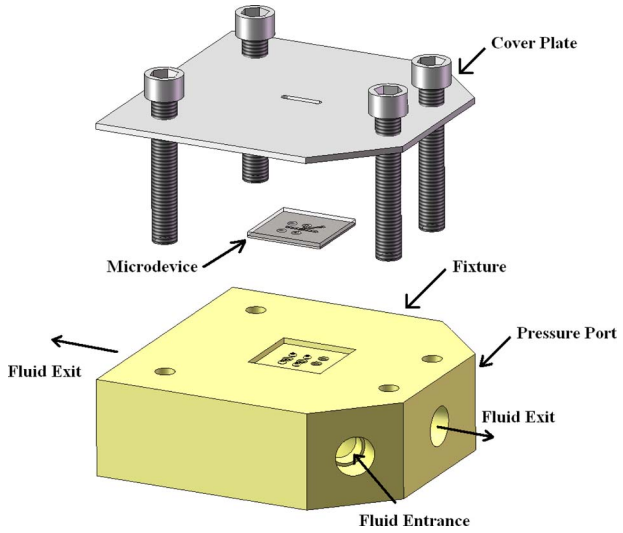

Fig. 2 Schematic of the assembly of the fixture, the microdevice and the cover plate

The microdevice was fabricated by anodically bonding and dicing two processed wafers. The two wafers were a silicon wafer etched using a deep reactive ion etcher (DRIE) to form the geometry of the channel and a Pyrex wafer with a thin-film metallic heater deposited on it. The fabrication of both wafers used photolithography carried out on a tool capable of back-side alignment.

The silicon wafer was first etched with a photoresist mask to a depth of 5 μm to create clearance for the heater vias and alignment marks. Next, 2 μm of oxide were deposited on both sides of the wafer in two separate steps providing oxide for hardmasks. DRIE was then performed on the top side using an oxide mask creating the channel 200 μm in depth. The orifice, fluid exit holes, and pass-through holes for the electrical contact pins were then etched from the bottom until they met the channel above.

The heater on the 1-mm thick Pyrex wafer was fabricated by depositing and patterning of metal layers and an oxide layer. First, 100 nm of titanium and 1 μm of aluminum were deposited without breaking vacuum. The 1-μm thick aluminum film was used to create vias and contact pads, while the underlying titanium existed in both those areas and the heater area. To electrically isolate and physically protect the heater, 1 μm of silicon oxide was deposited. The patterned silicon oxide film covers the heater and the vias but not the contact pads. In this way, the heater and the vias were electrically isolated from the water in the chamber, but electrical contact could be made with the spring-loaded contact pins outside of the chamber. Finally, the Pyrex and silicon wafers were anodically bonded together to form the completed microdevice.

The microdevice (Figs. 3 and 4) housed a channel 1.0 mm wide, 200 μm high, and 8.0 mm long into which the microjet flowed and impinged upon the heater from below. The microjet orifice was 67 μm in diameter, 250 μm long, and was positioned in the center of the bottom surface of the channel (silicon). The heater on the top surface of the channel (Pyrex) was square, measuring 80 μm on a side, and the center of the heater was aligned to the centerline of the microjet. This jet orientation (impingement on the heater from below) is different from most previous macroscale jet experiments, where the jet impinged on the heated surface from above. However, since the experiments presented here involved submerged jets, where the entire channel is flooded, in a channel only 200 μm tall and 1 mm wide, orientation is not expected to have a significant effect on performance.

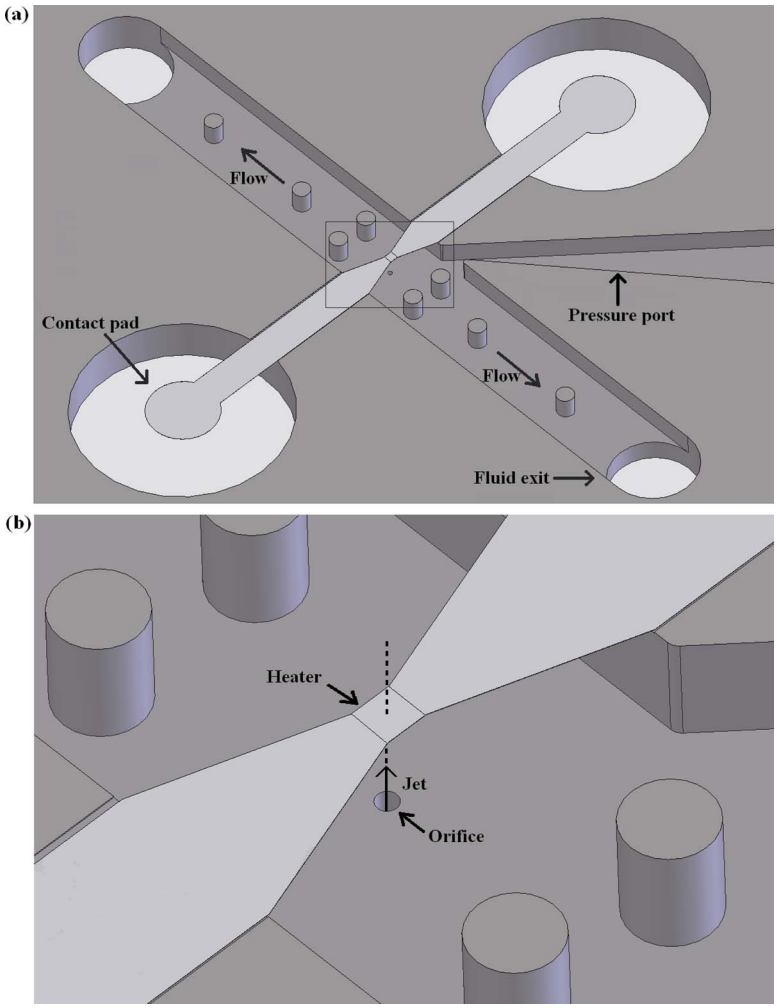

Fig. 3 (*a*) **Schematic of the microdevice and** (*b*) **a close up view of the orifice and the heater. The jet issues from the orifice in the center of the bottom surface of the channel. It impinges upon the heater 200** μ**m above (on the bottom surface of the Pyrex wafer), and the fluid exits down from either end of the channel.**

Fluid exited the channel at both ends through 1.0 mm holes in the bottom of the channel. During the experiments, the entire channel was flooded, creating a submerged jet. A pressure tap was located on a side wall in the middle of the channel to allow for measurement of chamber pressure. To enhance the structural integrity of the channel and to minimize deflection, several supporting pillars were fabricated in the channel starting more than 1 mm away from the orifice, such that their effect on the microjet was negligible.

2.2 Experimental Procedure. In addition to supplying heat to the system, the titanium heater also served as a thermistor. Before experiments were performed, the heater was placed in an oven, and its resistance was measured at 5°C intervals in the range 25–110°C. The temperature during this procedure was measured by a 36-gauge type-T thermocouple inserted into one of the fluid exit holes, positioning the thermocouple as close to the heater as possible. This thermocouple had previously been calibrated in a thermostatic bath with a precision resistance temperature detector (RTD) over the entire temperature range to an accuracy of ±0.2°C. A third-order polynomial curve was fit to these data to provide a relationship between resistance and average heater temperature. The measured data and curve fit are shown in Fig. 5.

The device was then placed into the fixture. The chamber in the

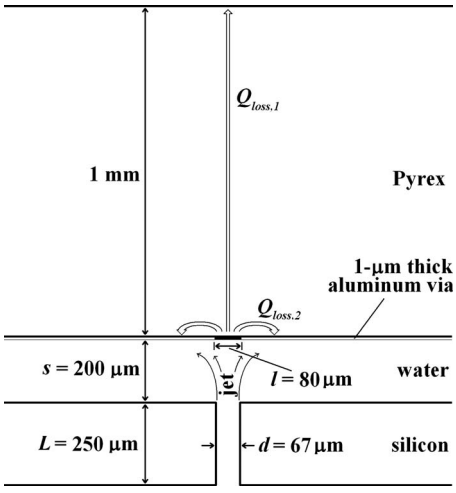

Fig. 4 Schematic showing the paths from the heater through which heat is lost. Most of the heat is lost through the path labeled $Q_{loss,2}$**, which cannot be measured independently or calculated without knowledge of local heat transfer coefficients.**

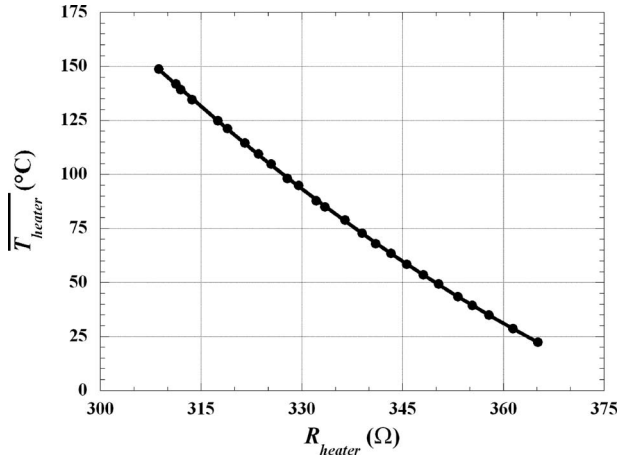

Fig. 5 Relationship between the resistance of the heater and average heater surface temperature. The error bars are smaller than symbol size.

device was evacuated, and power was supplied to the heater. The supplied voltage and current were measured, and an estimate of the heat lost through the fixture was obtained over the expected range of operating temperatures.

The supply tank was kept at a very low pressure with a vacuum pump for several days to ensure very low dissolved gas content in the de-ionized water used in the experiments. When water that had not been degassed as described above was used in earlier experiments, some gas bubbles could be seen on the downstream side of the orifice when large pressure drops were used. Immediately before the experiments were performed, the supply tank was pressurized with helium. Experiments were run at jet Reynolds numbers in the range $70 < \mathrm{Re}_d < 1900$ by controlling the flow rate through the system with the upstream needle valve and the pressure in the supply tank. At jet Reynolds numbers less than $\mathrm{Re}_d = 70$, the uncertainty in flow rate became very large. At $\mathrm{Re}_d = 1900$, the upstream pressure was 700 kPa absolute and higher jet Reynolds numbers were not attempted to prevent breakage of the device. Once a steady flow rate had been attained, a fixed voltage (~ 3 V) from the power supply was provided to the heater. Voltage and current were measured, and inlet pressure, inlet temperature, and chamber pressure were measured and recorded by a National Instruments data acquisition system.

2.3 Data Reduction. The jet Reynolds numbers were calculated according to

$$\mathrm{Re}_d = \frac{\rho \cdot V \cdot d}{\mu} \tag{1}$$

In this equation, ρ is the density, V is the average velocity at the orifice exit, d is the orifice diameter, and μ is the dynamic viscosity. The thermophysical properties of water were evaluated at the film temperature, which was calculated using

$$T_{\mathrm{film}} = \frac{T_s + T_{\mathrm{in}}}{2} \tag{2}$$

The orifice Reynolds numbers ($\mathrm{Re}_{d,o}$) were also calculated using Eq. (1). However, for the orifice Reynolds numbers, the thermophysical properties of water were evaluated at the orifice inlet temperature, which was approximately 22 °C for all of the experiments. Two different Reynolds numbers are necessary because the fluid properties at the orifice are relevant for the pressure drop behavior, and the fluid properties at the film temperature are used for the heat transfer behavior, consistent with previous work.

From the inlet and chamber pressures measured in the experiments, the pressure drop across the orifice was calculated. The relationship between pressure drop and flow rate through orifices can be presented in two ways: using the pressure loss coefficient K or the discharge coefficient C_d. The relationship between these parameters, flow velocity and pressure drop, is given by

$$K = \frac{(1-\beta^4)}{C_d^2} = \frac{\Delta P}{\frac{1}{2}\rho \cdot V^2} \tag{3}$$

where ΔP is the pressure drop across the orifice, and β is the ratio of the orifice diameter to the upstream tube diameter, which is effectively zero in the experiments presented here. The results presented in Sec. 3.1 are in terms of the pressure loss coefficient K, which, as can be seen in Eq. (3), is directly proportional to the pressure drop across the orifice.

The voltage and current supplied to the heater were used to calculate both the power dissipated by the heater and its resistance. The relationship between the electrical resistance of the heater and its average temperature was well characterized by calibration. The average surface temperature $\overline{T_s}$ was calculated from the total power supplied to the heater Q_{heater}, the heat loss estimate Q_{loss}, the heater area A_{heater}, the conductivity of silicon dioxide $k_{\mathrm{SiO_2}}$, the thickness of the silicon dioxide layer on the heater $t_{\mathrm{SiO_2}}$, and the average heater temperature $\overline{T_{\mathrm{heater}}}$ using

$$Q_{\mathrm{heater}} - Q_{\mathrm{loss}} = \frac{k_{\mathrm{SiO_2}} \cdot A_{\mathrm{heater}}(\overline{T_{\mathrm{heater}}} - \overline{T_s})}{t_{\mathrm{SiO_2}}} \tag{4}$$

From the total power supplied to the heater Q_{heater}, the heat loss estimate Q_{loss}, the heater area A_{heater}, the average heater surface temperature $\overline{T_s}$, and the inlet water temperature T_{in}, the area-averaged heat transfer coefficients over the heater $\overline{h}$ were calculated using

$$Q_{\mathrm{heater}} - Q_{\mathrm{loss}} = \overline{h} \cdot A_{\mathrm{heater}}(\overline{T_s} - T_{\mathrm{in}}) \tag{5}$$

Note that to comply with current practices in jet impingement heat transfer, we employed the commonly-used inlet temperature as the pertinent reference temperature in calculating the heat transfer coefficient and Nusselt number.

The area-averaged Nusselt numbers $\overline{\mathrm{Nu}_d}$ were calculated from the area-averaged heat transfer coefficient, the orifice diameter d, and the conductivity of water $k_{\mathrm{H_2O}}$ using

$$\overline{\mathrm{Nu}_d} = \frac{\overline{h} \cdot d}{k_{\mathrm{H_2O}}} \tag{6}$$

The conductivity of water used to calculate the Nusselt numbers was evaluated at the film temperature.

2.4 Heat Loss Estimation. As described above, before performing heat transfer experiments, the heat loss through the Pyrex wafer and the fixture was measured by completely evacuating the chamber and applying power to the heater. At steady state, the heater current and voltage were measured, and the power supplied to the heater and temperature of the heater were calculated. A polynomial was fit to these data to relate the heat lost from the back of the heater to its temperature. However, the path of heat losses (the amount of heat supplied which was not removed by convection over the surface of the heater) during the experiments is much different than the path present with the chamber evacuated. The heat loss measured in a vacuum neglects any heat lost by convection to the water from the surface of the Pyrex and the aluminum vias outside of the area covered by the heater. Therefore, the heat losses measured in a vacuum represent a best-case scenario.

To better understand heat losses during the experiment, a finite element analysis was performed using a commercially available software package, COMSOL MULTIPHYSICS. In this analysis, a 1-mm cube section of the Pyrex wafer was modeled. The 80-μm square heater was centered on the bottom face of this cube, and the

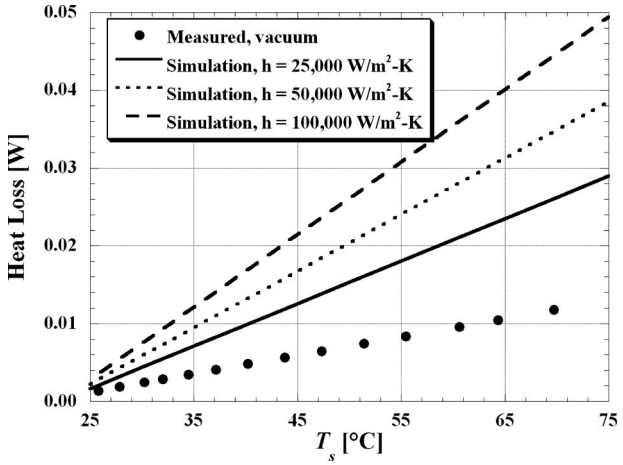

Fig. 6 Plot of the measured vacuum heat losses and the heat losses calculated using finite element analysis for several values of heat transfer coefficient. The error bars for the measured values are smaller than the symbol size.

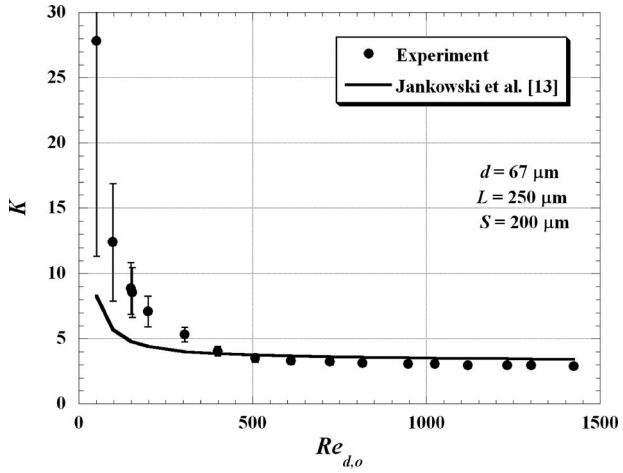

Fig. 7 The effect of Reynolds number on the pressure loss coefficient

aluminum vias and oxide layers were included in the model. A constant temperature boundary condition was applied to the heater, and a convection boundary condition was applied to the remainder of the surface exposed to the water, including the aluminum vias and exposed Pyrex sections. The inlet temperature of the water (which was the ambient temperature in these experiments, approximately 22°C) and a constant heat transfer coefficient were used in the simulation. To the remaining boundaries a constant temperature boundary condition at the ambient temperature was applied.

As shown in Fig. 6, the finite element analysis gave much higher estimated heat losses than were measured in the vacuum—more than double if the heat transfer coefficient is greater than 25,000 W/m^2 K. Moreover, the analysis showed that nearly all of the losses were not by conduction to the outside boundaries of the Pyrex ($Q_{loss,1}$ in Fig. 4), but rather by conduction from the back of the heater through the Pyrex to the surface of the Pyrex and aluminum vias, and then by convection to the water ($Q_{loss,2}$ in Fig. 4). Even though Pyrex is a very good insulator ($k=1.1$ W/m K), the heat flow needed to travel only miniscule distances (~ 10 μm) through the Pyrex to reach the surface just outside of the heater area, where the heat transfer coefficient is very large. Because of this low thermal resistance heat loss path, the calculated losses were on the order of the heat transfer from the heater directly to the fluid.

With the chosen boundary conditions, a worst-case estimate of the heat losses was obtained. In the actual experiments, the nonconvective boundaries of this volume were at some temperature above the ambient, reducing those conduction losses. The assumption of constant heat transfer coefficient on the surface of the Pyrex and vias also serves to give the worst-case estimate, since the literature on macroscale jets, as well as research of Wu et al. [9] and Patil and Narayanan [10] on microjets, suggest the heat transfer coefficient is greatest near the stagnation point and decreases with distance from the stagnation point. Therefore, the worst-case estimate overstates the losses, possibly significantly. The measured vacuum heat losses (best case) and the heat losses calculated using finite element analysis (worst case) are shown in Fig. 6.

The area-averaged Nusselt number results presented in the Sec. 3.2 are calculated using the assumption that the actual losses during the experiments, Q_{loss} in Eq. (5), are the arithmetic mean of the best and worst case losses described above. Since the worst case losses depend on the heat transfer coefficient, the solution is calculated iteratively. The uncertainty in the heat loss measurement is then taken to be one-half of the difference between the best case and worst case. This results in a quite large uncertainty in the area-averaged Nusselt number, but, as will be discussed below, the overall conclusion of the paper is not affected by this large value.

2.5 Uncertainties. The propagation of uncertainties for the reduced data followed standard methods [14]. The uncertainty in the Reynolds number (both jet and orifice) was less than $\pm 5\%$ for all experiments. The uncertainty in the area-averaged Nusselt number was approximately $\pm 85\%$ for the lowest Reynolds numbers and decreased to $\pm 65\%$ for the highest Reynolds numbers. This very large uncertainty is due almost entirely to the uncertainty in the heat losses described above. The large uncertainties reported in this investigation are inherent to the length scale of the heater. The heater was deposited on an excellent insulator with an extremely low thermal conductivity. However, due to the conjugate convection-conduction nature of the heat losses and the very small length scales involved, the heat losses are not experimentally measurable. A numerical simulation was undertaken to better understand these losses, but due to our very conservative approach (taking the uncertainty in heat losses to span the entire range from the best-to worst-case situations), the experimental uncertainty remained large. The uncertainty in the pressure loss coefficient was less than $\pm 35\%$ for all points except the smallest Reynolds number and less than $\pm 5\%$ for $Re_{d,o} > 400$.

3 Results and Discussion

3.1 Pressure Drop. The pressure loss coefficients determined from these experiments are shown in Fig. 7. For comparison purposes the correlation given by Jankowski et al. [13] is also shown. Error bars are included in the figure for all data points; however, the error bars are smaller than the symbol size for $Re_{d,o} > 500$. While the trend is the same, the experimentally determined pressure loss coefficients were larger than predicted by the model at low orifice Reynolds numbers. However, for $Re_{d,o} > 500$, the pressure loss coefficients were slightly less than predicted by the model.

The model of Jankowski et al. [13] assumes that the overall pressure drop in an orifice tube is the sum of the pressure drop due to friction in developing flow in a straight length of tube and the pressure drop due to flow through a sharp-edged (zero length) orifice, as shown by

$$\Delta P = K \cdot \frac{1}{2}\rho \cdot V^2 = (K_f + K_s) \cdot \frac{1}{2}\rho \cdot V^2 \tag{7}$$

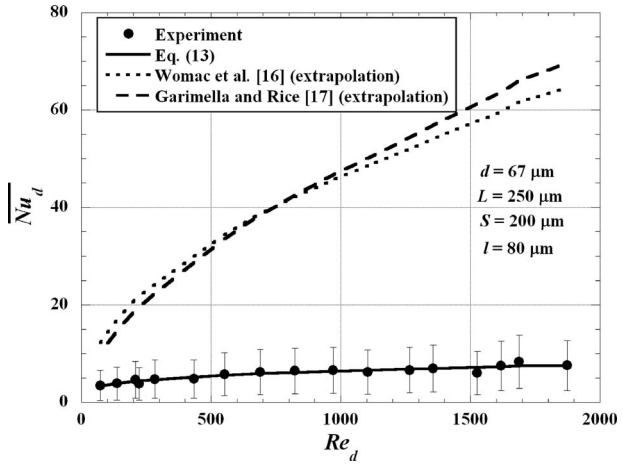

Fig. 8 The heat transfer performance of the microjet

The contribution due to flow friction was calculated using a correlation given by Shah [15], which is expressed as

$$K_f = f\frac{L}{d} = \frac{\Delta P_f}{\frac{1}{2}\rho \cdot V^2} = \frac{4}{\mathrm{Re}_{d,o}}\frac{L}{d}\left(\frac{3.44}{\sqrt{\xi}} + \frac{16 + 3.125/\xi - 3.44/\sqrt{\xi}}{1 + 0.000212/\xi^2}\right) \tag{8}$$

where f is the Darcy friction factor and $\xi = L/(d\ \mathrm{Re}_{d,o})$. Jankowski et al. [13] developed a correlation for the contribution due to flow through a sharp-edged orifice, expressed as

$$\frac{1}{\sqrt{K_s}} = C_{d,s} = 0.6\left[1 + \exp(-0.12\sqrt{\mathrm{Re}_{d,o}}) - 2.16\exp(-0.26\sqrt{\mathrm{Re}_{d,o}}) + 0.16\left(1 - \frac{\sqrt{\mathrm{Re}_{d,o}}}{1 + \sqrt{\mathrm{Re}_{d,o}}}\right)\right] \tag{9}$$

In the case of microjet flow, the presence of the impingement surface will also have an effect on the overall pressure drop. This effect is not represented in the model of Jankowski et al. [13]. The pressure loss coefficient from the experiment is larger than that predicted by the model at low orifice Reynolds numbers, suggesting that the pressure drop is increased due to the presence of the wall. At orifice Reynolds numbers in the range $\mathrm{Re}_{d,o} > 500$, however, the pressure loss coefficient is approximately 15% lower than the pressure drop for a sharp-edged orifice. The pressure drop for the impinging jet flow in this range is quite close to that predicted by the correlations for orifice flow. The presence of the wall onto which the jet impinges is likely to cause large recirculation zones and entrainment that are not present in typical orifice flows at low orifice Reynolds numbers. At higher orifice Reynolds numbers, both orifice and impinging jet flows are expected to cause recirculation zones and entrainment. This may explain why the pressure drop is not well predicted by the model at low orifice Reynolds numbers but agrees well for $\mathrm{Re}_{d,o} > 500$.

3.2 Heat Transfer. The observed Nusselt numbers are plotted in Fig. 8. For comparison purposes the correlations given by Womac et al. [16] and Garimella and Rice [17] have also been included in the figure. The experimental heat transfer coefficients ranged from 30,000 $\mathrm{W/m^2\,K}$ to 80,000 $\mathrm{W/m^2\,K}$. Both correlation curves shown in Fig. 8 are extrapolations, since they were developed from macroscale jet data. The 67-μm diameter is well outside of the geometrical range of these correlations. The Reynolds numbers investigated here are also below the range of data from which the correlations were developed. However, since no correlations for microscale jets exist in the literature, these correlations are the best available. The area-averaged Nusselt number correlation given by Womac et al. [16] for a jet is given by

$$\frac{\overline{\mathrm{Nu}_d}}{\mathrm{Pr}^{0.4}} = 0.785\ \mathrm{Re}_d^{0.5} A_r + 0.0257\ \mathrm{Re}_y^{0.8}\frac{d}{y}(1 - A_r) \tag{10}$$

where A_r is the ratio of the "impingement zone" area to the heater area given by the equation

$$A_r = \frac{\pi(1.9d)^2}{l^2} \tag{11}$$

and y is the average length of the wall-jet region. The authors state that A_r should be set to 1 when A_r as determined by Eq. (11) is greater than 1, as is the case with the geometry under investigation. Interestingly, Womac et al. divided the entire heat transfer area into two separate regions: the impingement zone, which is influenced directly by jet impingement and is taken to extend to a radius of $1.9d$, and the wall-jet region outside of the impingement zone. The impingement zone Nusselt number was taken to have a weaker dependence on the Reynolds number than did the wall-jet region. This correlation fit all of the data for which it was determined within $\pm 16\%$.

The correlation given by Garimella and Rice [17] is for the stagnation point Nusselt number, rather than an area-averaged Nusselt number, since the correlation given for area-averaged Nusselt numbers is specifically for a 10 mm $\times$ 10 mm area. Since the heater size is small in these experiments, the stagnation Nusselt number correlation is appropriate and is given by

$$\mathrm{Nu}_d = 0.492\ \mathrm{Re}_d^{0.585}\ \mathrm{Pr}^{0.4}\left(\frac{S}{d}\right)^{0.024}\left(\frac{L}{d}\right)^{-0.09} \tag{12}$$

The authors state that this correlation fit most of the data within $\pm 10\%$.

An extrapolation of the widely-used correlation given by Martin [1] could not be applied for this geometry. The Martin correlation is valid for area ratios (the ratio of orifice area to heater area) between 0.004 and 0.04. Because the area ratio investigated in these experiments is very large (0.55), the correlation gives a nonphysical negative value for Nusselt number.

Both correlations shown in Fig. 8 overpredict the area-averaged Nusselt number by 200–800%. The overprediction is not a result of the large uncertainties associated with the experiments. That is, even if the losses (which account for nearly all of the uncertainty) were assumed to be zero and all of the power provided to the heater was used to calculate the heat transfer coefficients, the correlations would still overpredict the area-averaged Nusselt numbers by up to 500%.

There could be several reasons for this disagreement. In the investigations of the performance of macroscale single jets, a long tube is usually used to provide the jet fluid. Because of the length of these tubes, the jet flow typically has the velocity profile of fully-developed flow in a tube. The L/d ratio of the orifice in this investigation is less than 4, and the flow in the orifice is not expected to be fully developed. The hydrodynamic entrance conditions of the jet are therefore different for this investigation than for the jet flows that have provided the data for the development of the correlations. The discrepancy reported here is, however, likely much larger than would be caused by differing entrance conditions.

The discrepancy in the size of the heater area relative to the area of the jet may explain some of the difference between the measured area-averaged Nusselt numbers and those predicted by the correlations. The jet in these experiments covered more than half of the heater area. In the two microjet investigations previously undertaken [9,10], the heat transfer coefficient was maximum at the stagnation point. However, several experimental studies of local jet impingement heat transfer at the macroscale have shown the existence of a local minimum of the heat transfer coefficient at the stagnation point [18–20]. In cases where this local minimum was observed, the heat transfer coefficient increased to a maximum at distances as large as 1.5 diameters away from the stagnation point (outside of the heater area in this experiment).

Since the area over which the area-averaged Nusselt numbers were measured in this experiment is small relative to the size of the jet, it is possible that the entire area was within the previously-observed zone of locally reduced heat transfer. Even if this were the case, however, this would account for only a small portion of the discrepancy between the measured area-averaged Nusselt numbers and the values predicted by the correlations.

Another possible cause for the disagreement between the experimental results and the correlations are some fundamental differences between jet flow at the microscale and at the macroscale. Since only orifice pressure drop and impingement zone heat transfer data have been collected in this experiment, this conclusion cannot be made on the basis of this work. Future work in which the fluid mechanics of the microscale jet flow is investigated should be undertaken.

The jet Reynolds numbers investigated here are smaller than those used to develop the correlations. Even though the velocities are large, the small diameter of the orifice in the microdevice leads to jet Reynolds numbers much lower than are typically seen in the macroscale jet flows that have been thoroughly studied. The correlations shown in Fig. 8 were therefore developed using data from almost exclusively turbulent jets, while the jets present in the microdevice under investigation were in the laminar regime. Therefore, the discrepancy may have been caused by flow regime differences between the experiment and the data used to develop the correlations. This is perhaps the most likely reason for the disagreement.

A curve fit to the experimentally obtained area-averaged Nusselt number is included in Fig. 8. The equation of this fit is given by

$$\overline{\mathrm{Nu}_d} = 0.635\ \mathrm{Re}_d^{0.245}\ \mathrm{Pr}^{0.4} \tag{13}$$

Only water was used in this experiment, so the Prandtl number exponent was set to 0.4, which is most often used in the jet literature [16,17]. This curve fit is valid only for the geometry studied here. Interestingly, this equation shows a much weaker dependence of the Nusselt number on the jet Reynolds number than is expected from earlier work. However, since the heater area is very close in size to the area of the orifice in this case, the area over which the Nusselt number is averaged is very close to the stagnation point. Some investigators, such as Womac et al. [16], Garimella and Rice [17], and Zhou and Ma [21] reported a weaker dependence on the jet Reynolds number for the stagnation point heat transfer coefficient than for the impingement surface far away from the stagnation point. The exponent reported here (0.245) is significantly lower than even those reported values (0.5, 0.585, and 0.5, respectively). Further research is required to determine the cause of this behavior.

4 Conclusions

An experimental investigation of the pressure drop and stagnation zone heat transfer coefficient of a single impinging microjet was undertaken. The pressure loss coefficients and area-averaged Nusselt numbers were reported over the range $50 < \mathrm{Re}_{d,o} < 1400$ and $70 < \mathrm{Re}_d < 1900$, respectively. The pressure loss coefficients obtained experimentally were much higher than predicted by the model of Jankowski et al. [13] at orifice Reynolds numbers less than 500 due to the presence of the impingement wall. At orifice Reynolds numbers higher than 500, the experimentally obtained pressure loss coefficients were well predicted by the model.

Even with the large experimental uncertainties taken into account, the observed area-averaged Nusselt numbers were significantly less than that predicted by Womac et al. [16] or Garimella and Rice [17]. The dependence of the area-averaged Nusselt number on the Reynolds number ($\mathrm{Nu}_d \propto \mathrm{Re}_d^{0.245}$) is also much weaker than has been previously observed. Additional experimentation should be undertaken to better understand whether the discrepancies noted above are due to the laminar flow regime investigated in these experiments or if the flow through microscale jets is fundamentally different from that through macroscale jets. In addition, we have initiated a numerical simulation project to explore these two issues, as well as the conjugate effects inherent with these very small length scales.

Acknowledgment

This work is supported by the Office of Naval Research (ONR) under the Multidisciplinary University Research Initiative (MURI) award No. GG10919. The authors would like to acknowledge the staff of the Micro and Nano Fabrication Clean Room (MNCR) at Rensselaer Polytechnic Institute for their assistance in fabrication of the test devices.

Nomenclature

English

A_{heater} = surface area of the heater (m^2)
A_r = ratio of impingement zone area to heater area
C_d = discharge coefficient of orifice
d = diameter of orifice (m)
f = Darcy friction factor
$\bar{h}$ = area-averaged convective heat transfer coefficient ($\mathrm{W/m^2\ K}$)
K = pressure loss coefficient
$k_{\mathrm{H_2O}}$ = thermal conductivity of water (W/m K)
$k_{\mathrm{SiO_2}}$ = thermal conductivity of silicon dioxide (W/m K)
L = length of orifice (m)
l = side length of heater (m)
Nu_d = Nusselt number
$\overline{\mathrm{Nu}_d}$ = area-averaged Nusselt number
ΔP = pressure drop (Pa)
Q_{heater} = total power supplied to the heater (W)
Q_{loss} = heat loss from heater other than convection directly to fluid (W)
$Q_{\mathrm{loss},1}$ = heat loss by conduction through the Pyrex to the ambient (W)
$Q_{\mathrm{loss},2}$ = heat loss by convection from the surface in contact with the water (W)
R_{heater} = resistance of the heater (Ω)
Re_d = jet Reynolds number
$\mathrm{Re}_{d,o}$ = orifice Reynolds number
Re_y = wall-jet Reynolds number
S = standoff (distance from orifice exit to heater surface) (m)
T_{in} = fluid inlet temperature (°C)
T_{film} = film temperature (°C)
$\overline{T_{\mathrm{heater}}}$ = average heater temperature (°C)
T_s = average surface temperature (°C)
$t_{\mathrm{SiO_2}}$ = thickness of silicon dioxide on heater (m)
y = average length of the wall-jet region (m)

Greek

β = ratio of orifice diameter to upstream tube diameter
μ = viscosity of water (kg/m s)
ξ = correlation parameter
ρ = density of water ($\mathrm{kg/m^3}$)

Subscripts

f = corresponding to developing flow in a tube
s = corresponding to flow through a sharp-edged orifice

References

[1] Martin, H., 1977, "Heat and Mass Transfer Between Impinging Gas Jets and Solid Surfaces," Adv. Heat Transfer, **13**, pp. 1–60.

[2] Jambunathan, K., Lai, E., Moss, M. A., and Button, B. L., 1992, "A Review of Heat Transfer Data for Single Circular Jet Impingement," Int. J. Heat Fluid Flow, **13**(2), pp. 106–115.
[3] Stefanescu, S., Mehregany, M., Leland, J., and Yerkes, K., 1999, "Micro Jet Array Heat Sink for Power Electronics," *Proceedings of the 12th IEEE International Conference on Micro Electro Mechanical Systems (MEMS)*, Orlando, FL, pp. 165–170.
[4] Fabbri, M., Jiang, S., and Dhir, V. K., 2003, "Experimental Investigation of Single-Phase Micro Jets Impingement Cooling for Electronic Applications," *Proceedings of the 2003 ASME Summer Heat Transfer Conference*, Las Vegas, NV, pp. 461–468.
[5] Wang, E. N., Zhang, L., Jiang, L., Koo, J.-M., Maveety, J. G., Sanchez, E. A., Goodson, K. E., and Kenny, T. W., 2004, "Micromachined Jets for Liquid Impingement Cooling of VLSI Chips," J. Microelectromech. Syst., **13**(5), pp. 833–842.
[6] Brunschwiler, T., Rothuizen, H., Fabbri, M., Kloter, U., Michel, B., Bezama, R. J., and Natarajan, G., 2006, "Direct Liquid Jet-Impingement Cooling With Micron-Sized Nozzle Array and Distributed Return Architecture," *Proceedings of the 10th Intersociety Conference on Thermal and Thermomechanical Phenomena and Emerging Technologies in Electronic Systems, iTherm 2006*, San Diego, CA, pp. 196–203.
[7] Sung, M. K., and Mudawar, I., 2008, "Single-Phase Hybrid Micro-Channel/Micro-Jet Impingement Cooling," Int. J. Heat Mass Transfer, **51**(17–18), pp. 4342–4352.
[8] Sung, M. K., and Mudawar, I., 2008, "Effects of Jet Pattern on Single-Phase Cooling Performance of Hybrid Micro-Channel/Micro-Circular-Jet-Impingement Thermal Management Scheme," Int. J. Heat Mass Transfer, **51**(19–20), pp. 4614–4627.
[9] Wu, S., Mai, J., Tai, Y. C., and Ho, C. M., 1999, "Micro Heat Exchanger by Using MEMS Impinging Jets," *Proceedings of the 12th IEEE International Conference on Micro Electro Mechanical Systems (MEMS)*, Orlando, FL, pp. 171–176.
[10] Patil, V. A., and Narayanan, V., 2005, "Spatially Resolved Heat Transfer Rates in an Impinging Circular Microscale Jet," Microscale Thermophys. Eng., **9**(2), pp. 183–197.
[11] Brutin, D., and Tadrist, L., 2003, "Experimental Friction Factor of a Liquid Flow in Microtubes," Phys. Fluids, **15**(3), pp. 653–661.
[12] Phares, D. J., Smedley, G. T., and Zhou, J., 2005, "Laminar Flow Resistance in Short Microtubes," Int. J. Heat Fluid Flow, **26**(3), pp. 506–512.
[13] Jankowski, T. A., Schmierer, E. N., Prenger, F. C., and Ashworth, S. P., 2008, "A Series Pressure Drop Representation for Flow Through Orifice Tubes," ASME J. Fluids Eng., **130**(5), p. 051204.
[14] Kline, S. J., and McClintock, F. A., 1953, "Describing Uncertainties in Single-Sample Experiments," Mech. Eng. (Am. Soc. Mech. Eng.), **75**(1), pp. 3–8.
[15] Shah, R. K., 1978, "Correlation for Laminar Hydrodynamic Entry Length Solutions for Circular and Noncircular Ducts," ASME J. Fluids Eng., **100**(2), pp. 177–179.
[16] Womac, D. J., Ramadhyani, S., and Incropera, F. P., 1993, "Correlating Equations for Impingement Cooling of Small Heat Sources With Single Circular Liquid Jets," ASME J. Heat Transfer, **115**(1), pp. 106–116.
[17] Garimella, S. V., and Rice, R. A., 1995, "Confined and Submerged Liquid Jet Impingement Heat Transfer," ASME J. Heat Transfer, **117**(4), pp. 871–877.
[18] Gardon, R., and Cobonpue, J., 1962, "Heat Transfer Between a Flat Plate and Jets of Air Impinging on It," International Developments in Heat Transfer, ASME, New York, pp. 454–460.
[19] Lytle, D., and Webb, B. W., 1994, "Air Jet Impingement Heat Transfer at Low Nozzle-Plate Spacings," Int. J. Heat Mass Transfer, **37**(12), pp. 1687–1697.
[20] Lee, J., and Lee, S.-J., 1999, "Stagnation Region Heat Transfer of a Turbulent Axisymmetric Jet Impingement," Exp. Heat Transfer, **12**(2), pp. 137–156.
[21] Zhou, D. W., and Ma, C. F., 2006, "Radial Heat Transfer Behavior of Impinging Submerged Circular Jets," Int. J. Heat Mass Transfer, **49**(9–10), pp. 1719–1722.